This article has been accepted for inclusion in a future issue of this journal. Content is final as presented, with the exception of pagination.

3D-Printed Multimode-Interference-Based Bessel Beamformer for Terahertz Dielectric Waveguides

Ashish Kumar, Surya Revanth Ayyagari, Muhsin Ali, Irmantas Kašalynas, *Senior Member, IEEE*, Daniel Headland, *Member, IEEE*, and Guillermo Carpintero, *Senior Member, IEEE*

***Abstract*—We demonstrate a Bessel beamformer based on multimode interference (MMI) for the terahertz (THz) wave range. Unlike traditional Bessel beam generation methods, which often rely on bulky free-space optical setups, our approach leverages a 3D-printed cyclic-olefin-copolymer (COC) MMI structure fed from a dielectric waveguide (DW) with a $\lambda/4$ slot-waveguide termination (SWT) that provides an index-matched interface for low reflection. Based on this interface and the low losses of the constituent materials, the beamformer achieves a measured transmission efficiency of 93.9% at 275 GHz, with a propagating distance of 20 mm (~20λ). Even at an extended distance of 35 mm (~35λ), the beam maintains a 50% efficiency. This approach addresses key limitations of existing free-space methods, offering a workable guided-wave approach to launch a THz Bessel beam.**

***Index Terms*—Bessel beam, cyclic olefin copolymer (CoC), multimode interference (MMI), slot waveguide termination (SWT), terahertz (THz).**

I. Introduction

BESSEL beams are nondiffracting waves, characterized by a Bessel-type radial intensity profile and a longitudinal line focus that can be sustained over a length of several wavelengths. As exact solutions to the Helmholtz equation, these waves propagate with minimal diffraction, preserving their spatial structure overextended distances without significant spreading [1], [2]. Their inherent self-healing properties, recovering intensity profiles after encountering obstacles, further broaden their utility [1]. In optics, Bessel beams enable applications such as particle trapping [1], optical manipulation [3], and nanofabrication [4]. At microwave frequencies, Bessel beams have been shown to underpin wireless power transfer [5], [6] and point-to-point secure communications [6], whereas at the terahertz (THz) range, they have demonstrated imaging [7], near-field communications [8], and THz computed tomography [9].

In the optical range, common approaches to launch a Bessel beam are the use of diffracting rings at the focal plane of a convergent lens [1], holographic methods [10], as well as axicon lenses [3], micro-optical element [11], and multimode optical fiber [12]. In the microwave range, by contrast, common approaches are to deploy radial line slot arrays [13], subsampled distributed arrays [14], and phased metasurfaces [15]. In the THz range, the most common approach to generate a Bessel beam has been to employ axicon conical lenses, which operates across a wideband frequency range from 3 to 7 THz, requiring bulky free-space optics [16]. Alternative approaches, such as plasmonic metasurfaces [17] and planar structures [18], are not as broadband, being typically designed for a specific frequency. THz Bessel beam generators shown to date rely mainly on free-space interference schemes, hindering compact systems. Recently, substrateless all-silicon microstructures have been shown as a suitable THz integration platform, based on low-index effective medium (EM) cladding for dielectric waveguides (DWs) [19]. Consequently, generating a Bessel beam from a THz DW could be highly advantageous over employing a nanojet generated by a cuboidal probe [20].

In this work, we adapt the optical-range multimode fiber-based Bessel beamformer [12] to the THz range. The THz signal in an all-intrinsic-silicon effective medium-clad substrateless dielectric waveguide (EMWG) [21], which offers low propagation loss of 0.05 dB/cm, >40% relative bandwidth, and planar all-Si fabrication for straightforward alignment [22], to a cylindrical 3D-printed low-loss cyclic-olefin-copolymer [23] multimode interference (COC-MMI) coupler [12]. The coupling between these two components is matched using a quarter-wave slot-waveguide termination (SWT) [24] that allows minimizing reflections, ensuring efficient coupling from the EMWG to the COC MMI. Experimental validation confirms 93.9% transmission efficiency over a 20λ propagation distance at 275 GHz. The modular structure provides a scal-

Received 6 November 2025; accepted 15 December 2025. This work was supported in part by the Terahertz Photonics for Communications, Space, Security, Radio-Astronomy, and Material Science (TERAOPTICS) Project under Grant 956857; in part by the Services Joint Undertaking through the European Union's (EU) Horizon Europe Research and Innovation Program TERA6G and the Horizon Europe Framework Program Project POLYNICES under Agreement 101096949 and Agreement 101070549; in part by the National Grant MiBiLab through MICIU/AEI/10.13039/501100011033 and European Regional Development Fund (ERDF)/European Union (EU) under Grant PID2023-149035OB-I00; and in part by the Ministerio de Asuntos Económicos y Transformación Digital and European Union-NextGenerationEU through the project "TERAcom-6G" within ÚNICO I+D 5G-6G 2023 Program for Research Infrastructure and Scientific Equipment under Grant TSI-064100-2023-39. The work of Daniel Headland was supported in part by Australian Research Council's Discover Early Career Researcher Award through Australian Government under Project DE240100625 and in part by the Article Processing Charge (APC): Universidad Carlos III de Madrid under Agreement CRUE-Madroño 2025. *(Corresponding author: Ashish Kumar.)*

Ashish Kumar and Guillermo Carpintero are with the Opto-electronics and Laser Technology Group, Department of Electronics technology, Universidad Carlos III de Madrid, 28911 Madrid, Spain (e-mail: akumar@ing.uc3m.es; guiller@ing.uc3m.es).

Surya Revanth Ayyagari and Irmantas Kašalynas are with the Institute of Applied Electrodynamics and Telecommunications, Vilnius University, 10257 Vilnius, Lithuania, and also with the Center for Physical Sciences and Technology (FTMC), 02300 Vilnius, Lithuania (e-mail: surya.revanth@ftmc.lt; irmantas.kasalynas@ftmc.lt).

Muhsin Ali is with LeapWave Technologies, 28919 Madrid, Spain (e-mail: muhsin.ali@leapwavetech.com).

Daniel Headland is with The University of Adelaide, Adelaide, SA 5005, Australia (e-mail: daniel.headland@adelaide.edu.au).

This article has supplementary downloadable material available at https://doi.org/10.1109/LMWT.2025.3647140, provided by the authors.

Digital Object Identifier 10.1109/LMWT.2025.3647140

© 2025 The Authors. This work is licensed under a Creative Commons Attribution 4.0 License.
For more information, see https://creativecommons.org/licenses/by/4.0/

This article has been accepted for inclusion in a future issue of this journal. Content is final as presented, with the exception of pagination.

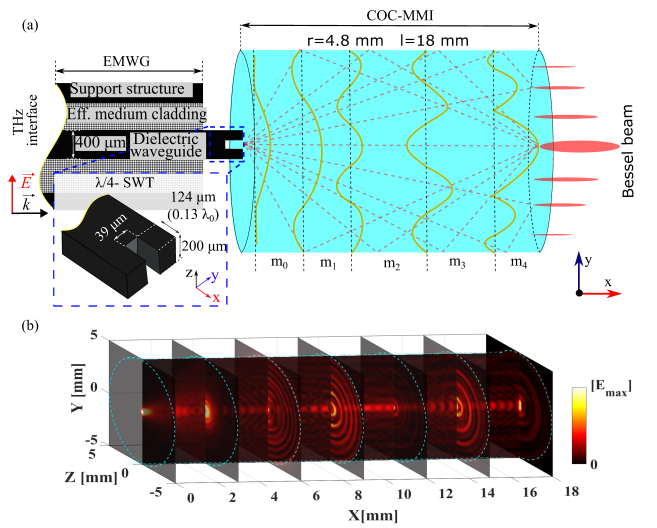

Fig. 1. (a) Schematic of the Bessel beamformer. (b) Simulated E-field distributions at multiple cross sections along the propagation axis showing interference pattern inside the COC-MMI, xy plot at $z = 0$ and zy along x-axis with an interval of 3 mm at 275 GHz.

able platform for various applications, nondestructive imaging, wireless power transfer, and communication link. The design supports mass production and compatibility with system integration.

II. Concept and Design

The proposed Bessel beamformer architecture is sketched in Fig. 1(a), showing its three key components: EMWG, COC-MMI, and SWT. The first element is the EMWG, a DW defined in a 200-μm-thick low-loss high-resistive silicon wafer with permittivity (ϵ_r) of 11.68 and loss tangent ($\tan\delta$) of 1.5×10^{-5} [25], with two main constituents: the waveguide core and the EM section. The waveguide core is 400 μm wide, $\sim\lambda/2$ at 275 GHz. The DW core is surrounded by an EM section, realized by a high-density array of subwavelength-sized through-holes in the silicon. We have used a diameter $d = 90$ μm and lattice period $a = 100$ μm, suitable for the used foundry and facilitating support area. For the TE polarization, which is parallel to the plane of the slab, the relative permittivity is approximated by [21]

$$\epsilon_y = \epsilon_{\mathrm{Si}} \frac{(\epsilon_0 + \epsilon_{\mathrm{Si}}) + (\epsilon_0 - \epsilon_{\mathrm{Si}})\,\zeta}{(\epsilon_0 + \epsilon_{\mathrm{Si}}) - (\epsilon_0 - \epsilon_{\mathrm{Si}})\,\zeta}\,, \qquad \zeta = \frac{\pi d^2}{2\sqrt{3}a^2}$$

where ϵ_0 and ϵ_{Si} are the relative permittivities of air and silicon, respectively, and ζ is the air fill factor within silicon. The following element in the dielectric Bessel beamformer is the COC-MMI section. It is a cylindrical structure defined in COC, with $\epsilon_r = 2.31$, $\tan\delta < 0.002$ [26], and low attenuation (~0.6 dB/mm) between 220 and 325 GHz [23]. This section supports a discrete set of cylindrical modes, excited by the TE_{01} mode on the EMWG. For $n = 0$, dominant azimuthal order excitation, the dominant azimuthal order is $n = 0$. The fields in the MMI can be expanded into Bessel functions of the first kind as $E(r,\varphi,x) = \sum_{m,n} A_{m,n} J_n(k_{r,m}(r)) e^{jn\varphi} e^{-j\beta_m x}$ for $0 \le r < R$ and $0 \le x \le L$, where $k_0 = (2\pi)/\lambda_0$ is the free-space wavenumber at 275 GHz and $n_{\mathrm{COC}} = \sqrt{\epsilon_r}$ is the refractive index of COC. The quantity $k_{r,m}$ denotes the mth radial wavenumber imposed by the cylindrical boundary condition at $r = R$, while $\beta_m = ((n_{\mathrm{COC}}k_0)^2 - k_{r,m}^2)^{1/2}$ is the corresponding longitudinal propagation constant [12]. The coefficients $A_{m,n}$ are the excitation amplitudes of each cylindrical mode. For azimuthally symmetric ($n = 0$), the aperture field at the MMI exit ($x = L$) reduces to $E_{\mathrm{out}}(r) = \sum_m A_m J_0(k_{r,m} r) e^{-j\beta_m L}$. With $R = 4.8$ mm (COC $\epsilon_r \sim 2.31$ at 275 GHz), the MMI supports 13 radial orders ($m = 1$–13), providing sufficient spectral density to synthesize a high-fidelity J_0-like aperture while avoiding excessive high-order loss. Setting $L = 18$ mm aligns the modal phases ($\beta_m L$) of the lowest orders at the exit, maximizing constructive interference into the central lobe and yielding a zeroth-order Bessel beam.

Since the EMWG feeds the THz signal into the COC-MMI and there is significant index contrast between these two media, we need to suppress index-mismatch reflections at the EMWG–MMI interface. To this end, we terminate the EMWG with an SWT, in which the slot width controls the effective modal index [27]. The slot width is chosen to set the effective modal index near $n_{\mathrm{eff,slot}} \sim (n_{\mathrm{Si}} n_{\mathrm{COC}})^{1/2}$, and the slot length L_s is set to $\lambda_g/4$ of the guided wavelength. Numerical simulation performed using CST Microwave Studio for a 400-μm-wide, 200-μm-thick DW, optimized at 275 GHz, indicates that a 39-μm slot width meets the index target, and $L_s = 124$ μm ($\sim\lambda_g/4$) implements a quarter-wave anti-reflection interface that minimizes back reflections.

To illustrate Bessel beamforming, Fig. 1(b) presents the E-field evolution in the COC MMI: a longitudinal xy profile ($z = 0$) and yz cross sections sampled every 3 mm along $x = 0$–18 mm. At the EMWG–MMI interface ($x = 0$ mm), a high-intensity spot appears from the SWT coupling. Between $x \approx 4$ and 9 mm, concentric rings emerge from MMI. By $x = 18$ mm, the field exhibits a well-formed zeroth-order Bessel pattern with a dominant central lobe and surrounding rings. The yz slices highlight three stages: initial collimation (0–3 mm), ring development (6–12 mm), and stabilization of the quasi-nondiffracting profile (15–18 mm). This spatial progression underscores the MMI structure's ability to systematically redistribute THz waves while suppressing higher order modes, enabling a stable zeroth-order Bessel beam.

III. Experiments and Results

The EMWG-SWT was fabricated via deep reactive ion etching (DRIE) on a 200-μm-thick silicon wafer. On the other hand, the COC-MMI cylinder was additively manufactured using COC filament with a high-precision 3-D printer by the fused deposition modeling technique at 245 °C, with a layer height of 50 μm and 100% infill to replicate the structural dimensions optimized via full-wave simulations accurately. Further information on tolerance and packaging is detailed in the supplementary information. The fabricated Bessel beamformer was assembled within a 3D-printed COC mount, designed with alignment holes for precise EMWG positioning and a standard rectangular waveguide (WR) circular flange interface to couple the COC-MMI structure. The assembly configuration is schematically depicted in Fig. 2(a), with a physical prototype photograph provided in Fig. 2(b). The Bessel beamformer assembly was fed from a rectangular hollow metallic waveguide to interface the EMWG with the THz signal source. The EMWG's other side is terminated with a quarter-wave SWT tip matched with free space [24], which

This article has been accepted for inclusion in a future issue of this journal. Content is final as presented, with the exception of pagination.

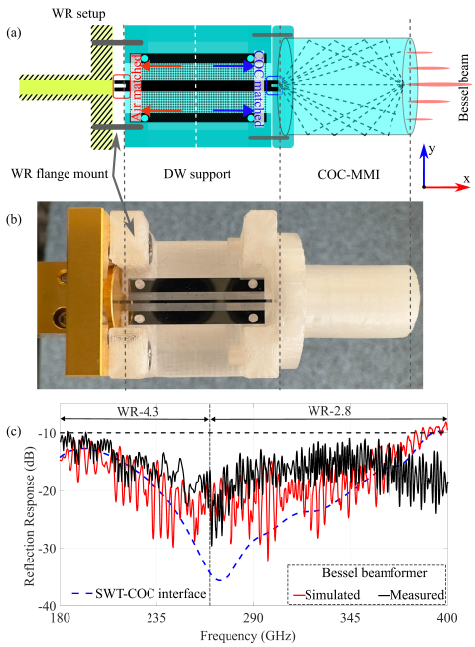

Fig. 2. (a) Schematic of the WR feed experimental setup. (b) Photograph of experimental setup. (c) Reflection response.

enables coupling to a Hollow waveguide [28], ensuring the efficient excitation of the fundamental mode from the WR. In addition, SWT configuration helped to maintain the compactness of the module by eliminating the conventionally used long-tapered-based feeding into or out of WR. To characterize the assembled module, we used an Anritsu VectorStar vector network analyzer (VNA), equipped with VDI WR-4.3 and WR-2.8 extension heads operating across the 180–400-GHz band. The matching performance of the beamformer was determined by measuring the reflection response of the assembly, with a focus on its two key interfaces: the transition from WR to SWT-EMWG and from EMWG-SWT to COC-MMI. As shown in Fig. 2(c), the simulated reflection response of the SWT-COC interface reaches −35 dB and remains below −10 dB across the 180–400-GHz frequency band, while the Bessel beamformer response stays below −10 dB.

For the beam profile measurement, a free-space THz setup operating at 275 GHz was implemented. As illustrated in the schematic in Fig. 3(a), this setup uses a COC aspherical lens to focus a collimated free-space beam onto the SWT-EMWG, with a Ti-microbolometer [29] serving as the detector for our Bessel beamformer output. An additional 3D-printed support was added to the one previously shown in Fig. 3(b) for stability. While this configuration showcases the versatility of SWT in accepting signals from either standard WR or free-space interfaces, it presents a practical challenge: the positioning accuracy of the extension heads is limited by the cable length and the difficulty of maintaining calibration during displacement.

Fig. 3(c) and (d) presents the simulated and measured beam profiles of the Bessel beamformer, illustrating how the intensity spreads along the optical axis in the *xy* plane and the cross section at the *yz* plane with varying distances of 20, 25, and 35 mm. The *xy* profile shows a dominant central lobe at $y = 0$, and the *yz* profile shows a maximum near $(y, z) = 0$ with visible outer rings, confirming the generation of a zeroth-order Bessel beam.

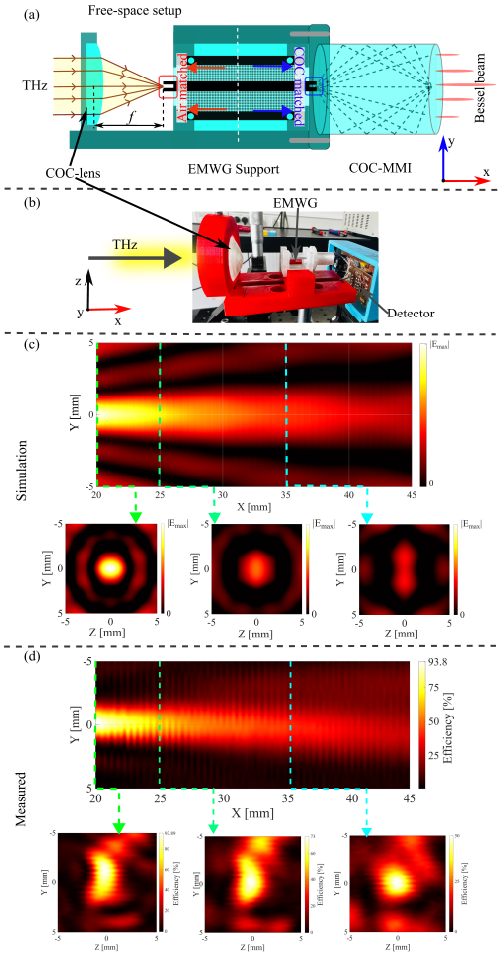

Fig. 3. (a) Schematic of the free-space feed experimental setup. (b) Photograph of the free-space experimental setup at 275 GHz. Beam profile along *xy* plane from 20 to 45 mm at *z*-axis = 0 and *yz* plane at $x = 20$, 25, and 35 mm. (c) Simulated beam profile. (d) Measured beam profile.

We quantified the Bessel beam efficiency using the lock-in voltage as a linear proxy for power under constant load/current. A reference signal of 6.55 mV was measured at $x = 20$ mm in the *yz* plane without the beamformer. With the beamformer introduced, the transmitted voltages and corresponding efficiencies $\eta = V_{\text{out}}/V_{\text{ref}}$ were: 6.15 mV at 20 mm (~93.9%), 4.78 mV at 25 mm (~73.0%), and 3.33 mV at 35 mm (~50.8%). These results confirm the beamformer's ability to maintain a nondiffracting profile overextended propagation lengths while highlighting the tradeoff between efficiency and propagation distance. The experimental beam profiles, measured at 20 mm from the COC-MMI output, agree with simulated distributions shown in Fig. 3(c) and (d), exhibiting a dominant central lobe, which is characteristic of a zeroth-order Bessel beam. Minor deviations, such as a marginally broader experimental lobe, arise from surface roughness and alignment of the free-space setup. Despite these practical challenges, the persistent central lobe confirms Bessel beam integrity under real-world conditions. The initial beam profile was measured 20 mm from the beamformer aperture to protect the beamformer package and the detector.

IV. Conclusion

We have introduced a compact nondiffracting Bessel beamformer for THz waveguides, combining an EMWG-SWT with

This article has been accepted for inclusion in a future issue of this journal. Content is final as presented, with the exception of pagination.

TABLE I
COMPARISON OF VARIOUS BESSEL BEAMFORMERS IN THE THZ RANGE

Technique	Freq. (THz)	NDR	Efficiency	Feed Type
Axicon [16] lens	3-7	$\sim 253\lambda$	–	Collimated beam
Plasmonic metasurface [17]	0.29	$\sim 20\lambda$	–	Focused beam
Planar structures [18]	0.9-1	$\sim 27\lambda$	40-58%	Collimated beam
Terajet [20]	0.3	$\sim 2\lambda$	–	Collimated beam
EMWG-SWT-(MMI) (This work)	0.18-0.4	$\sim 44\lambda$	93.4% at 20λ 50% at 35λ	Collimated beam or WR

a COC-MMI cylinder. These components are fabricated using intrinsic silicon and COC to ensure low-loss performance. In addition, the use of $\lambda/4$ slot matched terminations provides index matching from silicon to COC that minimizes the reflection losses. Furthermore, the slot-based termination contributes to the overall compactness of the device. The experimental confirmation of the Bessel beam generation at 275 GHz shows a measured efficiency of 93.9% after approximately $\sim 20\lambda$ of propagation.

Table I compares the performance and feed type. The results conclude that our work is the first of its kind demonstration of Bessel beamformer fed with EMWG-SWT with efficient performance considering compactness and nondiffractive range (NDR). This compact beamformer maintains a narrow beamwidth while conserving energy overextended distances, making it ideal for THz applications such as contactless probing, sensing, and resilient narrow-beam coupling.

REFERENCES

[1] J. Durnin, J. J. Miceli, and J. H. Eberly, "Diffraction-free beams," *Phys. Rev. Lett.*, vol. 58, no. 15, pp. 1499–1501, Apr. 1987.

[2] J. Durnin, "Exact solutions for nondiffracting beams i the scalar theory," *J. Opt. Soc. Am. A*, vol. 4, no. 4, p. 651, Apr. 1987.

[3] R. M. Herman and T. A. Wiggins, "Production and uses of diffractionless beams," *J. Opt. Soc. Amer. A, Opt. Image Sci.*, vol. 8, no. 6, pp. 932–942, Jun. 1991.

[4] D. Fan, L. Wang, and Y. Ekinci, "Nanolithography using Bessel beams of extreme ultraviolet wavelength," *Sci. Rep.*, vol. 6, no. 1, Aug. 2016, Art. no. 31301.

[5] F. Benassi, W. Fuscaldo, D. Masotti, A. Galli, and A. Costanzo, "Wireless power transfer in the radiative near-field through resonant Bessel-beam launchers at millimeter waves," in *Proc. IEEE Wireless Power Transf. Conf. (WPTC)*, Jun. 2021, pp. 1–4.

[6] E. Negri, W. Fuscaldo, P. Burghignoli, and A. Galli, "Leaky-wave analysis of TM-, TE-, and hybrid-polarized aperture-fed Bessel-beam launchers for wireless-power-transfer links," *IEEE Trans. Antennas Propag.*, vol. 71, no. 2, pp. 1424–1436, Feb. 2023.

[7] S. F. Busch, G. E. Town, M. Scheller, and M. Koch, "Focus free terahertz reflection imaging and tomography with Bessel beams," *J. Infr., Millim., THz Waves*, vol. 36, no. 3, pp. 318–326, Mar. 2015.

[8] I. V. A. K. Reddy, D. Bodet, A. Singh, V. Petrov, C. Liberale, and J. M. Jornet, "Ultrabroadband terahertz-band communications with self-healing Bessel beams," *Commun. Eng.*, vol. 2, no. 1, Oct. 2023, Art. no. 70.

[9] A. Bitman, S. Goldring, I. Moshe, and Z. Zalevsky, "Computed tomography using broadband Bessel THz beams and phase contrast," *Opt. Lett.*, vol. 39, no. 7, pp. 1925–1928, 2014.

[10] J. Turunen, A. Vasara, and A. T. Friberg, "Holographic generation of diffraction-free beams," *Appl. Opt.*, vol. 27, no. 19, pp. 3959–3962, 1988.

[11] I. V. A. K. Reddy, A. Bertoncini, and C. Liberale, "3D-printed fiber-based zeroth- and high-order Bessel beam generator," *Optica*, vol. 9, no. 6, pp. 645–651, 2022.

[12] X. Zhu, A. Schülzgen, L. Li, and N. Peyghambarian, "Generation of controllable nondiffracting beams using multimode optical fibers," *Appl. Phys. Lett.*, vol. 94, no. 20, May 2009, Art. no. 201102.

[13] A. Mazzinghi et al., "Large depth of field pseudo-Bessel beam generation with a RLSA antenna," *IEEE Trans. Antennas Propag.*, vol. 62, no. 8, pp. 3911–3919, Aug. 2014.

[14] P. Lemaitre-Auger, S. Abielmona, and C. Caloz, "Generation of Bessel beams by two-dimensional antenna arrays using subsampled distributions," *IEEE Trans. Antennas Propag.*, vol. 61, no. 4, pp. 1838–1849, Apr. 2013.

[15] Y. C. Zhong and Y. J. Cheng, "Ka-band wideband large depth-of-field beam generation through a phase shifting surface antenna," *IEEE Trans. Antennas Propag.*, vol. 64, no. 12, pp. 5038–5045, Dec. 2016.

[16] K. Miyamoto, R. Nomura, S. Tsurumaru, and T. Omatsu, "Tunable terahertz Bessel beams with orbital angular momentum," *Opt. Continuum*, vol. 1, no. 4, pp. 633–640, 2022.

[17] Y. Monnai, D. Jahn, W. Withayachumnankul, M. Koch, and H. Shinoda, "Terahertz plasmonic Bessel beamformer," *Appl. Phys. Lett.*, vol. 106, no. 2, Jan. 2015, Art. no. 021101.

[18] S. Liu et al., "Anomalous refraction and nondiffractive Bessel-beam generation of terahertz waves through transmission-type coding metasurfaces," *ACS Photon.*, vol. 3, no. 10, pp. 1968–1977, Oct. 2016.

[19] D. Headland, M. Fujita, G. Carpintero, T. Nagatsuma, and W. Withayachumnankul, "Terahertz integration platforms using substrateless all-silicon microstructures," *APL Photon.*, vol. 8, no. 9, Sep. 2023, Art. no. 091101.

[20] S. Hisatake and E. Miyake, "Terahertz scanning microscopy with 2λ depth of field based on photonic nanojet generated by a dielectric cuboid probe," *Opt. Exp.*, vol. 30, pp. 45303–45311, Dec. 2022.

[21] W. Gao, X. Yu, M. Fujita, T. Nagatsuma, C. Fumeaux, and W. Withayachumnankul, "Effective-medium-cladded dielectric waveguides for terahertz waves," *Opt. Exp.*, vol. 27, no. 26, pp. 38721–38734, Dec. 2019.

[22] R. Koala, R. Maru, K. Iyoda, L. Yi, M. Fujita, and T. Nagatsuma, "Ultra-low-loss and broadband all-silicon dielectric waveguides for WR-1 band (0.75–1.1 THz) modules," *Photonics*, vol. 9, no. 8, p. 515, Jul. 2022.

[23] S. F. Busch, M. Weidenbach, J. C. Balzer, and M. Koch, "THz optics 3D printed with TOPAS," *J. Infr., Millim., Terahertz Waves*, vol. 37, no. 4, pp. 303–307, Apr. 2016.

[24] D. Headland, A. Kumar, H. Lees, W. Withayachumnankul, and G. Carpintero, "Matched dielectric slot waveguide as an all-dielectric terahertz magnetic dipole," *Opt. Lett.*, vol. 49, no. 5, pp. 1361–1364, 2024.

[25] J. Dai, J. Zhang, W. Zhang, and D. Grischkowsky, "Terahertz time-domain spectroscopy characterization of the far-infrared absorption and index of refraction of high-resistivity, float-zone silicon," *J. Opt. Soc. Amer. B, Opt. Phys.*, vol. 21, no. 7, pp. 1379–1386, Jul. 2004.

[26] A. Sengupta, A. Bandyopadhyay, B. F. Bowden, J. A. Harrington, and J. F. Federici, "Characterisation of olefin copolymers using terahertz spectroscopy," *Electron. Lett.*, vol. 42, no. 25, pp. 1477–1479, Dec. 2006.

[27] Z. Zheng, M. Iqbal, and J. Liu, "Dispersion characteristics of SOI-based slot optical waveguides," *Opt. Commun.*, vol. 281, no. 20, pp. 5151–5155, Oct. 2008.

[28] A. Kumar, M. Ali, D. Headland, and G. Carpintero, "Compact and robust silicon waveguide to hollow metallic waveguide coupling using a quarter-wave dielectric slot waveguide for mmW and THz waves," in *Proc. Int. Topical Meeting Microw. Photon. (MWP)*, Oct. 2023, pp. 1–4.

[29] L. Qi et al., "Antenna-coupled titanium microbolometers: Application for precise control of radiation patterns in terahertz time-domain systems," *Sensors*, vol. 21, no. 10, p. 3510, May 2021.